Investigation of Corrosion Inhibitor Adsorption on Mica and Mild Steel Using Electrochemical Atomic Force Microscopy and Molecular Simulations

Huiru Wang,[,**] Sumit Sharma,[**] Alain Pailleret,[‡,*] Bruce Brown,[**] and Srdjan Nešić[‡,**]*

Electrochemical atomic force microscopy (EC-AFM) experiments, including simultaneous linear polarization resistance (LPR) tests and in situ AFM imaging, under a CO_2 atmosphere, were performed to investigate the adsorption characteristics and inhibition effects of a tetradecyldimethylbenzylammonium corrosion inhibitor model compound. When the inhibitor bulk concentration was at 0.5 critical micelle concentration (CMC), in situ AFM results indicated nonuniform tilted monolayer formation on the mica surface and EC-AFM results indicated partial corrosion of the UNS G10180 steel surface. At 2 CMC, a uniform tilted bilayer or perpendicular monolayer was detected on mica, and corrosion with UNS G10180 steel was uniformly retarded. Consistently, simultaneous LPR tests showed that corrosion rates decreased as the inhibitor concentration increased until it reached the surface saturation value (1 and 2 CMC). Molecular simulations have been performed to study the formation of the inhibitor layer and its molecular-level structure. Simulation results showed that at the initiation of the adsorption process, islands of adsorbed inhibitor molecules appear on the surface. These islands grow and coalesce to become a complete self-assembled layer.

KEY WORDS: carbon steel, cementite, corrosion inhibitors, CO_2 corrosion, electrochemical atomic force microscopy, molecular simulations, quaternary ammonium

INTRODUCTION

Carbon steel is widely used as the primary material for the construction of oil and gas transmission pipelines. While carbon steel has excellent mechanical properties and low cost, it is susceptible to corrosion attack in typical service environments where water is invariably present along with crude oil and gas. Corrosion-related accidents have been responsible for heavy economic losses, risks to life, and environmental pollution. Amphiphilic ionic surfactants containing polar head group moieties, including nitrogen, oxygen, phosphorus and/or sulfur, and an alkyl tail, have been shown to exhibit excellent corrosion inhibition properties even at low concentrations (ppm level), and so are commonly used as corrosion inhibitors for mild steel.[1]

The corrosion inhibition efficiency of these inhibitor molecules is linked to their strong tendency to adsorb at metal/water interfaces. The adsorption behavior of corrosion inhibitors depends on their affinity for the metal interface,[2] surfactant chemistry,[3] and bulk inhibitor concentration.[4] It is important to understand how the nature of the adsorbed layer and surface coverage of corrosion inhibitors vary with their bulk concentration as this allows for optimizing the number of corrosion inhibitors needed in field applications. Previous work has focused on measuring corrosion rates at different inhibitor concentrations.[5-6] These traditional electrochemical methods only provide information about corrosion rates averaged over the whole surface but do not provide any information about the mechanism behind corrosion inhibition, and neither do they detect localized or nonuniform corrosion.[7] Atomic force microscopy (AFM) fills this gap as it allows direct imaging of adsorbed layers on various substrates, including metallic surfaces, with a nanometric resolution.

Previous AFM studies of quaternary ammonium surfactants on mica surfaces have demonstrated that the adsorption morphology varies from spherical micelles, and meandering cylindrical micelles to featureless bilayers, as the length of the alkyl tail and types of counterion are varied.[8-9] Molecular simulations of surfactant adsorption have revealed that both the head group size and intermolecular hydrophobic interactions influence the nature of the adsorbed layer and its morphology.[10-11]

Woodward, et al.,[12] studied the growth kinetics of octadecylphosphonic acid-based self-assembled monolayers (SAMs) on mica by ex situ AFM imaging of an incomplete surface layer, and reported the formation of adsorbed surfactant islands. The adsorption process was proposed to comprise nucleation followed by growth and coalescence of the islands. Other studies using ex situ AFM to study the growth of adsorbed SAMs have reported similar nucleation and growth mechanisms.[13-15]

Most AFM studies of surfactant adsorption have been performed on a mica surface. Although similar adsorption

Submitted for publication: June 2, 2022. Revised and accepted: August 11, 2022. Preprint available online: August 11, 2022, https://doi.org/10.5006/4136.
‡ Corresponding authors. E-mail: alain.pailleret@sorbonne-universite.fr; nesic@ohio.edu.
* Sorbonne Université, CNRS, Laboratoire Interfaces et Systèmes Electrochimiques (LISE, UMR 8235), 4 place Jussieu, (case courrier 133), 75005, Paris, France.
** Institute for Corrosion and Multiphase Technology, Department of Chemical & Biomolecular Engineering, Ohio University, 342 West State Street, Athens, Ohio 45701.

ISSN 0010-9312 (print), 1938-159X (online)

behavior has been observed on inert metallic surfaces, such as gold,[16-17] there are very few in situ AFM studies of surfactant adsorption on carbon steel due to the dramatic alteration of surface topography caused by corrosion during the measurements.[18-19] However, it is important to study carbon steel as a substrate in order to examine the effect of adsorption of corrosion inhibitors on these surfaces considering its corrosion is a severe problem in the oil and gas industry. Although quaternary ammonium type inhibitors are widely used as corrosion inhibitors, their adsorption and inhibition mechanisms on carbon steel are incompletely understood. In this work, in situ electrochemical AFM investigations have been performed to study the effect of bulk concentration of a quaternary ammonium corrosion inhibitor model compound on the nature of the adsorbed layer formed on mica and G10180 (UNS G10180[(1)]), including determining its inhibitive effect on CO_2 corrosion of carbon steel. To complement the experiments, molecular simulations have been used to understand the molecular-level organization of this corrosion inhibitor in the adsorbed layer and study the kinetics of the formation of these layers.

EXPERIMENTAL PROCEDURES

2.1 | Synthesis of Corrosion Inhibitor Model Compounds

In order to obtain required molecular structures and purities, model quaternary ammonium inhibitors with varying tail lengths are routinely synthesized, as bromide salts, and characterized by our group.[20-21] The model compound used in this work consisted of a polar head group, dimethylbenzylammonium, and a hydrophobic tail comprising 14 carbon atoms: tetradecyl ($-C_{14}H_{17}$), as shown in Figure 1 and termed BDA-C14. The representative synthesis reaction for this series of model compounds is described in previous work.[21-22] Proton nuclear magnetic resonance (^{1}H-NMR) spectroscopy was used to characterize the synthesized model compounds, which showed them to be recovered at 99% purity levels. The detailed characterization procedure has been reported in a previous publication by our group.[22] By using a pure, well-defined surfactant-type organic corrosion inhibitor such as the one selected in this study, the mechanism of corrosion mitigation can be better understood and modeled.

2.2 | Materials and Solutions

Mica, being an atomically smooth and polar surface, was used in the first part of this study. Mica is composed of negatively charged aluminosilicate layers in which the excess negative charge arises from the substitution of tetrahedrally coordinated Si^{4+} by Al^{3+}.[23] These layers are neutralized and kept together by electrostatically bound potassium cations (K^+). Half of them are randomly associated with each of the two opposing surfaces after cleavage and can be exchanged for other cations in aqueous solutions,[24] which can produce strong electrostatic interactions favorable for the adsorption of quaternary ammonium-type corrosion inhibitors. In this study, before each new AFM experiment, mica was mechanically cleaved to produce clean and inherently flat surfaces with a roughness of the order of 0.2 nm.

(1) UNS numbers are listed in *Metals & Alloys in the Unified Numbering System*, published by the Society of Automotive Engineers (SAE International) and cosponsored by ASTM International.

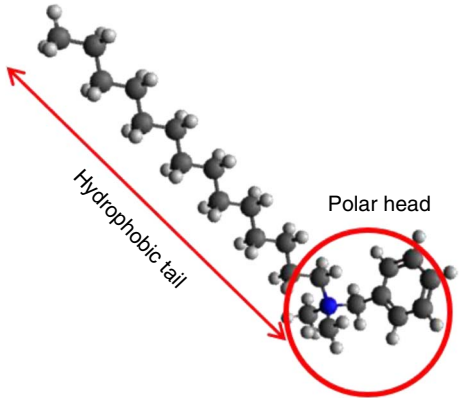

FIGURE 1. *Molecular structure of tetradecylbenzyldimethylammonium (BDA-C14).*

The steel specimens were cut from a pipeline sample made of UNS G10180 carbon steel (the steel composition is listed in Table S1 in Supplemental Material), and successively abraded using 400, 600, 800, and 1200 grit silicon carbide papers followed by 9 μm, 3 μm, and 1 μm diamond particle loaded paste on a polishing cloth. They were then washed with acetone, ethanol, and water and then dried in the air, which leads to the formation of a (sub)-nanometric oxide layer through slight oxidation of the steel surface that induces a surface polarity.

Different bulk concentrations of the inhibitor were selected: 0 ppm (blank), 25 ppm (0.5 CMC), 50 ppm (1 CMC), and 100 ppm (2 CMC). Here, CMC stands for critical micelle concentration. The CMC of BDA-C14 was determined by measuring changes in surface tension of aqueous solution of BDA-C14 as a function of concentration using the du Noüy ring method with a Krüss tensiometer,[25] solutions of 1 wt% NaCl-containing BDA-C14 were prepared using deionized water with a conductivity of 18 $M\Omega \cdot cm^{-1}$. The solution was deoxygenated by sparging with CO_2 for at least 2 h before beginning the experiments, CO_2 was continuously introduced during the measurements. Experiments were conducted at room temperature (25°C), and the initial pH of the test electrolye was 3.9. The test matrix was shown in Table 1.

Table 1. *Experimental Conditions*

Parameter	Value
Materials	Mica, UNS G10180 carbon steel
Inhibitor model compounds	Tetradecylbenzyldimethylammonium (BDA-C14)
Critical micelle concentration	50 ppm
Inhibitor concentrations	0 CMC (0 ppm) 0.5 CMC (25 ppm) 1 CMC (50 ppm) 2 CMC (100 ppm)
NaCl concentration	1 wt%
Temperature	25°C
Initial pH	3.9
Atmosphere	CO_2 saturated
Techniques	Contact mode EC-AFM imaging, nanoscratching, and force curves, scanning electron microscopy (SEM)

2.3 | In Situ Contact Mode Atomic Force Microscopy Measurements

AFM measurements were performed in situ in aqueous solutions containing various concentrations of the inhibitor, using the commercial molecular imaging atomic force microscope system (i.e., a Pico-LE base and a PicoScan 2100[†] controller) in contact mode to achieve imaging and nanoscratching of the inhibitor film. Measurements were made at the substrate (mica or carbon steel)/aqueous solution interface in order to determine the structure of the adsorbed layer and surface coverage. Each AFM image required approximately the same amount of time (20 min) for a full scan unless specified. The scan rate of the AFM probe was set to 1,000 nm/s for a 1 μm × 1 μm scan area on mica. On UNS G10180 carbon steel, the general scan rate was set to 8,000 nm/s for a 10 μm × 10 μm scan area. A resolution of 512 × 512 pixels was adopted for all AFM images. The AFM tips used in these investigations (HYDRA-ALL-G-50[†], AppNano) were made of silicon and were mounted on triangular cantilevers with nominal spring constants of 0.284 N/m for nano-scratching tests on mica and 0.049 N/m for imaging on UNS G10180 carbon steel. Inhibitor layers could be imaged repeatedly without causing tip-induced damage using a low load (<2 nN) and during imaging the force setpoint has been set as 0. Inhibitors can also be scratched off of the substrate surface by repeatedly scanning the layer at a much higher load.[26] The detailed procedure of scratching experiments has been introduced in a previous publication.[27]

2.4 | In Situ Linear Polarization Resistance-Contact Mode Atomic Force Microscopy Measurements (Electrochemical Atomic Force Microscopy)

A custom-made AFM sample holder with a three-electrode cell configuration (shown in Figure S1 in Supplemental Material) was used for EC-AFM measurements, i.e., linear polarization resistance (LPR) measurements which are performed in parallel with in situ AFM experiments on the identical sample surface at the same time. AISI 316L stainless steel and UNS G10180 carbon steel were used as counter-electrode and working electrode materials, respectively. A KCl saturated AgCl/Ag reference electrode was placed in a compartment separated from the main cell by a Vycor®[†] membrane.[28] LPR was used to obtain corrosion rates by polarizing the working electrode from −10 mV to +10 mV with respect to the corrosion potential at a scan rate of 0.125 mV/s. A value of B = 26 mV/decade was used to convert the polarization resistance into a corrosion current and corrosion rate, based on a previous mechanistic study of CO_2 corrosion in inhibited systems.[29] Tafel slopes and corrosion rates were recorded by methods described in this previous study.[29]

2.5 | Molecular Simulations of Adsorption of Corrosion Inhibitors

To complement the experiments, molecular simulations were performed to study the adsorption of the selected corrosion inhibitor on polar surfaces. The corrosion inhibitor was modeled as an amphiphilic molecule with a linear alkyl tail. The goal of the simulations was to study the formation and the molecular-level arrangement of planar adsorbed layers of corrosion inhibitors, which are difficult to ascertain in experiments. In molecular simulations, motion of every atom in the system of interest is simulated numerically. Every atom applies a distance-dependent force on every other atom around it. This force depends on the nature of the atom. The distance-dependent molecular forces are numerically integrated in time. Self-assembly of adsorbed corrosion inhibitor molecules involves a large number of molecules organizing in ordered structures. Such a collective behavior occurs over long molecular time scales. These large systems and long time scales are efficiently studied using coarse-grained (CG) modeling, wherein chemical details of individual atoms are ignored. Rather, certain groups of atoms are represented by a single entity called a "bead". This CG approach significantly reduces the computational expense and thus allows the study of long-time scale behavior of a large number of molecules. In our CG description of a corrosion inhibitor molecule, the entire polar group is represented by one bead, and the alkyl tail is represented by a string of beads connected by bonds. Such a CG system is designed to capture two basic features: (a) strong affinity of the polar beads for the metal surface and (b) hydrophobic interactions between the alkyl beads of the inhibitor molecules. A detailed description of this model can be found in a previous publication.[10] Salient features of the utilized CG model are described as follows.

Every CG corrosion inhibitor molecule is a linear, semi-flexible string of beads. The bonds and angles between the beads are modeled by harmonic potential functions. To incorporate the hydrophobic effect, the interactions between the alkyl beads forming the tail of the corrosion inhibitor molecules are modeled using a Lennard-Jones (LJ) potential function.[30] The solid surface is represented by a smooth plane that strongly attracts the polar head bead of the corrosion inhibitor molecules. The interaction between the surface and the polar beads is modeled as a 9-3 potential function, which is the functional form obtained by integrating the interactions from a semi-infinite lattice of LJ atoms.[30] Previous works have revealed that amphiphilic molecules adsorb on mica in the standing-up configuration, suggesting that the interactions of the polar groups with the mica surface are much stronger than that of the alkyl groups.[31-32] Therefore, we set the interactions between the alkyl beads and the surface to zero in the CG model. In this simulation system, the surface occupies one face (z = 0) of the simulation box. The opposite face of the simulation box is modeled as a reflective surface to keep the volume of the system finite. Periodic boundary conditions are used on the other faces of the simulation box. The effect of water is incorporated by performing Langevin dynamics simulation.[30]

As is customary, reduced units are used in the simulations, as for molecular scale dimensions using standard units, i.e., specifying length in meters or energy in Joules, is not the most convenient choice. Rather, custom length, energy, and mass units are defined for a given molecular system. For the system studied herein, we set the size of one alkyl bead (the length parameter of the LJ potential) σ = 1. We set the value of thermal energy, $k_BT = 1$ and the mass of one alkyl bead, m = 1. The potential well-depth of the so-called "9-3 potential" is set to 5 k_BT. This value is similar to the binding energy of polar moieties on a metal surface calculated using density functional theory (DFT).[33] The potential well-depth of the LJ interaction between two alkyl beads is set to 0.065 k_BT. This value ensures that the total hydrophobic interaction between two alkyl tails is close to k_BT. The bond length between adjacent beads within a molecule is set to 0.3 σ. In the Langevin dynamics simulations, the time-step is chosen to be 0.001 $\sigma(m/k_BT)^{1/2}$. The force constants for bond and angle harmonic potentials are 100 k_BT/σ^2 and 50 $k_BT/\text{radians}^2$, respectively. The size of the simulation box is 20 σ × 20 σ × 40 σ. The total number of corrosion inhibitor

[†] Trade name.

molecules in the system is 400. We have confirmed the invariability of our simulation results in a larger system with 800 molecules and simulation box size of 20 σ × 20 σ × 80 σ.

RESULTS AND DISCUSSION

3.1 | In Situ Monitoring of Inhibitor Adsorption on Mica: Atomic Force Microscopy Nanoscratching and Force Curves

In a preliminary set of experiments, in situ AFM images were obtained in a 1 wt% NaCl aqueous electrolyte in the absence and in the presence of the inhibitor (Supplemental Material—Figures S2[a] and [b], respectively). All of the images are featureless, indicating that in situ AFM imaging can sometimes give ambiguous results when it comes to detecting adsorption of the inhibitor on mica. Therefore, AFM nanoscratching tests and force curves were performed to investigate the properties of the adsorbed inhibitor film.

In order to further investigate the structure of the adsorbed layers, the thickness of the adsorbed layer for the 0.5 CMC and 2 CMC inhibitor concentrations was measured by performing AFM nanoscratching tests in which a small area of the inhibitor layer (200 nm × 200 nm) was removed from the underlying mica substrate by repeatedly scanning at a critical normal force (the critical force selection procedure is shown in Figure S3 and with corresponding text in Supplemental Material). The nanoscratching of the surface resulted in the formation of a scratching print (hole) with uniform depth[26-27] on the condition that the normal force applied during the nanoscratching step was high enough: 20±1 nN for 0.5 CMC and 24±1 nN for 2 CMC (see Figures 2[a] and [b]). Subsequently, the height difference between scratched and nonscratched areas was determined from the surface profiles, which corresponds to the inhibitor film thickness. From these nanoscratching experiments, it is found that the layer thickness of inhibitor on mica at 0.5 CMC concentration is approximately 0.8±0.1 nm, which is about half of one molecular length of the alkyl tail (1.64 nm). It is generally assumed that if inhibitor molecules adsorb perpendicularly on the substrate surface to form a monolayer, the thickness of this monolayer should be equal to the alkyl tail length. Therefore, considering the inhibitor film thickness measured by AFM (~0.8 nm) (see Figure 2[a]) is smaller than the tail length (1.64 nm), it is concluded that the inhibitor molecules must have adsorbed as a tilted monolayer on the mica surface, as illustrated in the schematic description in Figure 2(c). The molecular orientation seen in Figure 2(c) was suggested by previous all-atom molecular dynamics simulation results.[34]

The same AFM nanoscratching tests were performed at a 2 CMC concentration (see Figure 2[b]). Scratching features with a measurable depth, like the one observed at a 0.5 CMC concentration (see Figure 2[a]), were observed in the AFM images. After measurement of the height profile, the layer thickness formed on mica at 2 CMC was determined to be 1.5±0.1 nm, which is about twice the film thickness of the tilted monolayer at 0.5 CMC (0.8±0.1 nm, see Figure 2[a]), indicating a bilayer with a tilted orientation is likely (see schematic illustration in Figure 2[d]) to form on mica for a 2 CMC bulk concentration. The alkyl tails in this bilayer (partly) overlap with each other due to hydrophobic interactions as found by previous molecular simulation results[10] and shown in the schematic description Figure 2(d). One imidazoline type of inhibitor has also been reported to have the monolayer formation at 0.5 CMC and bilayer formation at 2 CMC.[27] While the titled bilayer orientation of the molecules appears to explain the observation, one cannot rule out the possibility of a perpendicularly adsorbed monolayer at 2 CMC (as shown in Figure 2[d]) because the layer thickness (1.5 ±0.1 nm) is comparable to the molecular tail length (1.64 nm).

Repeated nanoscratching tests at 2 CMC with the same 24±1 nN normal force were conducted at many different locations on the mica surface and consistent layer thickness results were obtained, indicating that a uniform tilted bilayer or uniform perpendicular monolayer formed on the entire mica surface. This was not the case for a 0.5 CMC, as in some locations of the mica surface the tilted monolayer was not detected by nanoscratching. Instead, a very different picture emerged: an island (with a positive height contrast) was observed instead of a hole (with a negative height contrast) in the AFM images obtained after a nanoscratching step (see Figure S4 in Supplemental Material). Repeated experiments on multiple samples of mica all showed the same phenomenon, i.e., the two different topography features obtained after nanoscratching tests at 0.5 CMC. This indicates that the tilted monolayer formed on mica at 0.5 CMC was nonuniform.

Figure 3 shows the force-distance curves measured on inhibitor layers formed on mica from 1 wt% NaCl solution in the presence of inhibitor at 0.5 CMC and 2 CMC. Force curves were also performed on bare mica in 1 wt% NaCl solution (analysis is below Figure S5 in Supplemental Material) to compare with the curves obtained on inhibitor layers. In the presence of an inhibitor layer formed at 2 CMC, the tip experienced no force at large separations between the tip and surface, as observed in Figure 3 (see the red-dashed curve). As the tip approached the mica surface, there was an increasing repulsive force, which can only be caused by the indentation of a soft and self-assembled (well-ordered) inhibitor layer, by the AFM tip.[27,35] The repulsive force increased as the tip pushed closer towards the surface until a point called "breakthrough"[36] where there is a sudden decrease of the force as the tip penetrates the inhibitor layer. The corresponding force at the "breakthrough" penetration force was measured to be around 0.8±0.1 nN. After the tip penetrated through the layer, a further approach is easier and eventually caused contact between the tip and the stiff underlying mica surface,[37] as illustrated by the linear part of the force curves that is identical to the one obtained on bare mica. Multiple force curve tests on different locations of the mica surface had repeatable features (see Figure S5[c]), which indicates undoubtedly the existence of a uniform inhibitor layer on the entire mica surface for the bulk inhibitor concentration of 2 CMC.

In the case of 0.5 CMC, the AFM force curves (see Figure 3 blue curve) were qualitatively similar to those obtained in a 2 CMC solution but with a smaller penetration force (around 0.4 nN, what is half of the penetration force obtained at 2 CMC). The fact that the penetration force at 2 CMC is twice the penetration force at 0.5 CMC agrees with the tilted bilayer formation at 2 CMC and tilted monolayer formation at 0.5 CMC determined by nanoscratching tests. The nonuniform features of the layer formed on mica at 0.5 CMC have also been detected by force curves, as shown in Figure S5(b) in the Supplemental Material. Based on the above discussion, it can be concluded that a uniform tilted bilayer or perpendicular monolayer formed at 2 CMC while a nonuniform tilted monolayer formed at 0.5 CMC on the mica surface. This result is consistent with previous in situ AFM studies of surfactant adsorption that were shown to proceed via two different stages.[12,14-15,38] There is an initial nucleation period, wherein rapid adsorption of BDA-C14 at the mica surface is driven by electrostatic attractions between the cationic species and anionic lattice sites existing on mica at random positions. After the nucleation, a loosely packed sub-monolayer of adsorbed

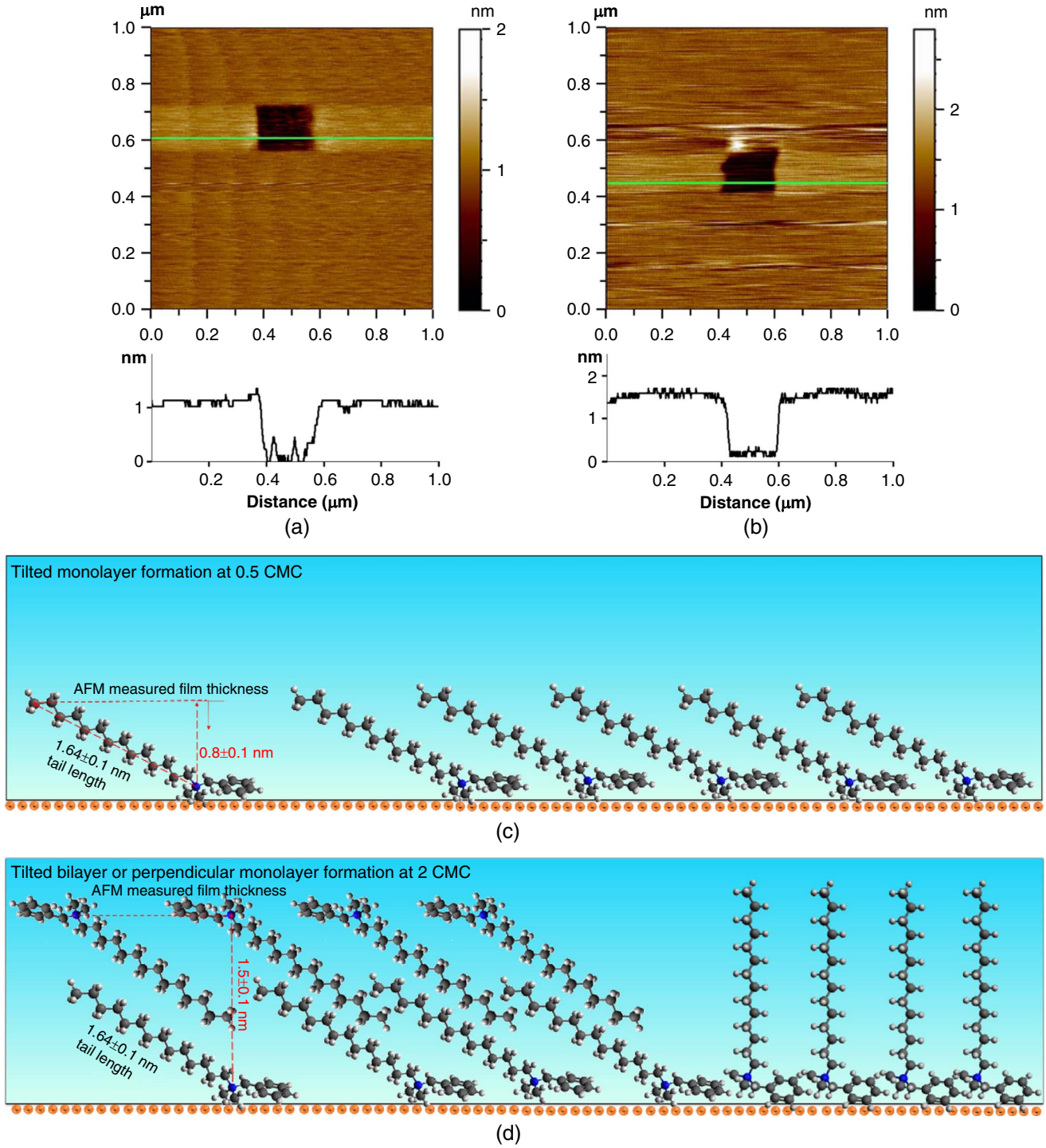

FIGURE 2. *Topography images obtained after nanoscratching steps performed on inhibitor layers formed on mica: (a) at 0.5 CMC and (b) at 2 CMC. The lower schematics show likely molecular orientation in the case of: (c) a tilted monolayer formed at 0.5 CMC and (d) a tilted bilayer or perpendicular monolayer formed at 2 CMC. (The layer thickness was determined by measuring the height difference between scratched and unscratched areas on a height profile. Height profiles were plotted along the green line appearing at the corresponding topography image.)*

BDA-C14 is formed on the surface, which then grows due to the coalescence of isolated islands together to form a self-assembled layer. Meanwhile, other sites remained sparingly covered by disordered and loosely distributed inhibitor molecules due to the low concentration of the inhibitor in the solution (0.5 CMC). At higher concentrations (1 CMC and 2 CMC), however, uniform coverage of the surface is achieved.

3.2 | Molecular Simulations of Corrosion Inhibitor Adsorption

The AFM experiments described above provide interesting insights into the adsorption behavior of a corrosion inhibitor model compound on mica at different concentrations. Concrete conclusions were made, but certain fundamental questions persist that need more in-depth analysis. Why do

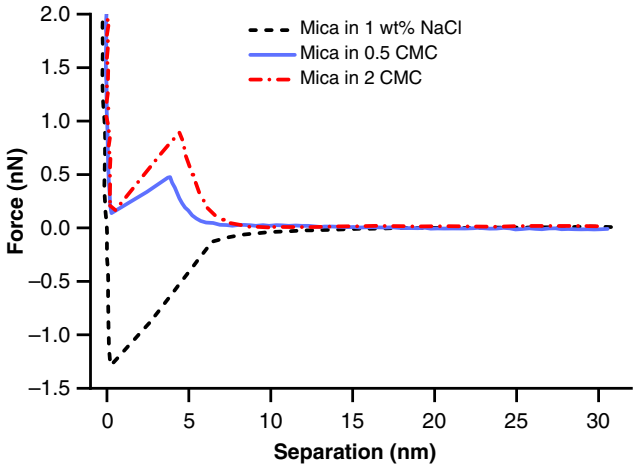

FIGURE 3. *Force curves measured on mica surface in the absence and presence of inhibitor (only the approach part of these curves is shown here).*

the molecules adsorb in patches rather than uniformly? Why does this happen only at low concentrations? What is the exact structural arrangement of the molecules in the adsorbed layer? What is the growth process of the adsorbed layer? In order to better answer these questions and understand the molecular-level details of the formation and structure of adsorbed corrosion inhibitor layers, for the experiments on mica using in situ AFM and reported above in *In Situ Monitoring of Inhibitor Adsorption on Mica: Atomic Force Microscopy Nanoscratching and Force Curves* section, CG simulations of adsorption of corrosion inhibitors on polar surfaces, such as mica, were performed. In previous work, co-authors of this manuscript developed a theoretical model to predict adsorbed configurations of corrosion inhibitors on polar surfaces.[39] The model revealed that the molecules adsorb by standing up on the surface unless the alkyl tails have an appreciable affinity for the surface, which results in the molecules adsorbing by lying flat on the surface. Previous experiments have shown that amphiphilic molecules adsorb on mica in the standing-up configuration.[31-32] These experiments suggest that alkyl tails do not have a strong affinity for the mica surface. This conclusion is also supported by fully atomistic simulations of adsorption of surfactants on mica.[40] To be reminded, in this CG model, the corrosion inhibitor molecules were represented by a linear arrangement of beads, with the first bead representing the polar head group and the remaining beads representing the alkyl tails. The affinity of the alkyl tails for the surface was set to zero. It was observed in simulations that the adsorption proceeds via the formation of patches (islands) of adsorbed molecules standing up on the surface.

Figure 4(a) shows the calculated decline in the number of patches of adsorbed molecules as a function of the extent of adsorption. A large number of patches appeared during the initial stages of adsorption. The corrosion inhibitor molecules adsorb in the perpendicular orientation to the surface because of the strong affinity of the polar group with the surface. The molecules adsorb in patches because of the favorable hydrophobic interactions between the alkyl tails.[11] As the adsorption proceeded further, these patches grew and coalesced with each other to eventually form a continuous layer. The extent of adsorption is defined as the fraction of the equilibrium concentration of adsorbed molecules. Islands of adsorbed molecules were identified by using the density-based spatial clustering of applications with noise (DBSCAN) algorithm.[10,41] During the times of patchy adsorption, localized areas of adsorbed molecules form because of the attractive hydrophobic interactions between the alkyl tails of the inhibitor molecules. Therefore, one can conclude that the patches of BDA-C14 molecules detected at 0.5 CMC on mica in the in situ AFM studies reported above, in *In Situ Monitoring of Inhibitor Adsorption on Mica: Atomic Force Microscopy Nanoscratching and Force Curves* section, are also formed due to these hydrophobic interactions. Due to the small size of the simulation system, the size of the observed patches is much smaller than those observed in the experiments. At the final stages of the adsorption in the simulations, the corrosion inhibitor molecules of this type are readily adsorbed in a uniform self-assembled layer on the surface.

Figure 4(b) shows a calculated snapshot of the adsorbed corrosion inhibitor layer, and Figure 4(c) shows the distribution of the center-of-mass of the corrosion inhibitor molecules in the equilibrium adsorbed configuration. The snapshot of the inhibitor layer and the distribution of molecules reveal that the molecules are arranged in a patchy bilayer with one sharp peak at a distance of 3.8 σ indicating the first layer and a small peak at a distance of 4.9 σ indicating the second layer.

The local arrangement of the molecules in the adsorbed layer can be studied by calculating the radial distribution function, g(r) in the xy plane (that is, the plane of the surface) of the adsorbed molecules.[33] Figure 4(d) shows the g(r), calculated by determining the average number of molecules at a distance r in the xy plane from a molecule, normalized by the density expected in a uniform distribution. The regular peaks in the g(r) indicate that the molecules in the adsorbed layer were arranged with a long-range order. As the magnitude of the peaks decreases as r increases, this implies that while the adsorbed layer had more structure than a typical liquid, it was still fluid-like and not well structured.

The molecular simulation results complement the experiments and conclusions reported in *In Situ Monitoring of Inhibitor Adsorption on Mica: Atomic Force Microscopy Nanoscratching and Force Curves* section by providing insights into kinetics of the adsorption process and the molecular-level structure of the adsorbed inhibitor layers, information that is difficult to obtain from direct experiments such as in situ AFM investigations. However, there are certain limitations of molecular simulations which need to be mentioned. First, while adsorption occurs on timescales of a few seconds to hours, molecular simulations can only sample timescales of, at most, a few microseconds. Therefore, in order to accelerate the adsorption process, much higher concentrations are used in molecular simulations. In one sense, this approach ignores the long timescales associated with the diffusion of the molecules towards the surface, and only captures the adsorption phenomenon when the local concentration of the inhibitors near the surface is high. A second limitation of simulations is with respect to the length scales that can be studied. Typically, simulations can only study length scales of a few 100 nm, because the computational complexity increases linearly with the number of particles in the system. Therefore, the simulations cannot capture the formation of macroscopic regions comprising uniformly adsorbed layers and bare surfaces.

At this stage, a fairly good description of: (i) the adsorption process of ionic surfactant-type corrosion inhibitors on the polar surface of mica; and (ii) the morphology of the resulting ionic surfactant-based deposits was established by

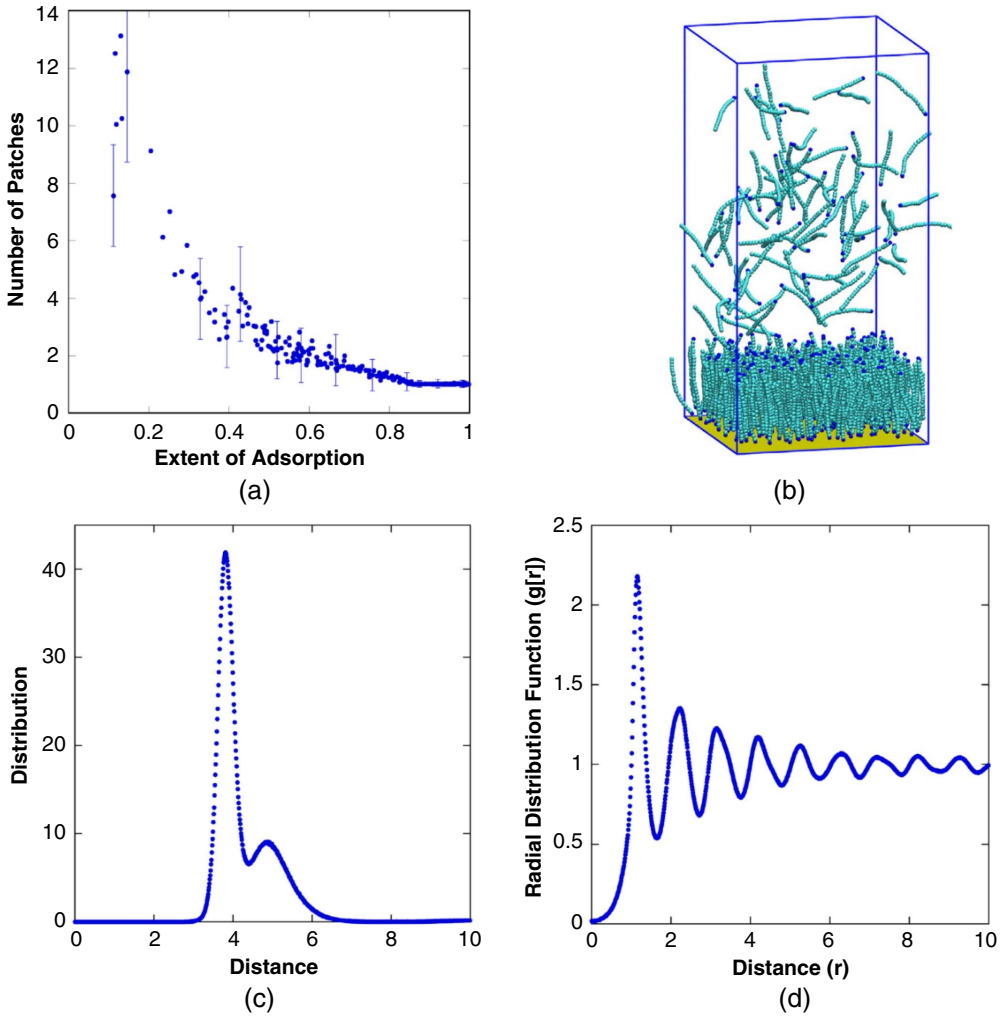

FIGURE 4. *Simulation results: (a) Number of distinct patches of adsorbed corrosion inhibitor molecules during the adsorption process observed in simulations. Adsorption begins by the appearance of patches of adsorbed molecules on the bare surface. Over time, these patches grow and coalesce and finally cover the entire surface. (b) A snapshot of the equilibrium configuration of adsorbed corrosion inhibitor molecules. The blue-colored beads represent the polar head and the cyan-colored beads represent the alkyl tail. The corrosion inhibitor molecules self-assemble in a fully formed first layer with their polar head toward the surface and a partially formed second layer in which the adsorbed molecules are interdigitated in the first layer with their polar head away from the surface. (c) Distribution of the center-of-mass of corrosion inhibitor molecules as a function of distance from the surface. The distribution shows that the adsorbed molecules form a monolayer with a partially formed interdigitated second layer. (d) Radial distribution function in the xy plane, g(r) of corrosion inhibitor molecules in the adsorbed layer showing signatures of an ordered arrangement of molecules.*

associating in situ AFM investigations with CG molecular simulations. These preliminary results can be correlated with the adsorption behavior of this corrosion inhibitor on the polar surface of slightly oxidized UNS G10180 steel and indicate how this could be related to inhibition efficiency, as discussed below, knowing that this is the real target of the investigations reported in this manuscript.

3.3 | In Situ Monitoring of Corrosion Inhibition on UNS G10180 Steel

3.3.1 | Linear Polarization Resistance Corrosion Rates Measurements

Figure 5 shows the LPR corrosion rate measurements in 1 wt% NaCl aqueous electrolyte at different times for various inhibitor bulk solution concentrations. They were performed in a custom-made AFM cell (see Figure S1 in Supplemental Material). It can be observed that, whatever the concentration, the corrosion rate initially diminishes rapidly with time, before it levels off at a relatively constant value for the remainder of the inhibition experiment. It is thought that during the initial phase, the inhibitor is adsorbing on the steel surface, which leads to an increase in the surface coverage and therefore to better inhibition of corrosion as a function of time. The stable value of the corrosion rate reached after long exposure decreased when the inhibitor bulk concentration is increased, initially quite dramatically, but as higher concentrations were reached, there was less and less change. This result agrees with the theory described by Hackerman, et al., showing that the amount of adsorbed inhibitor on the metal surface approached a maximum at a certain bulk solution concentration, termed surface saturation concentration.[42-43] No more effective adsorption should be expected once the surface saturation concentration is reached, which would result in no further obvious decrease in the corrosion rate.

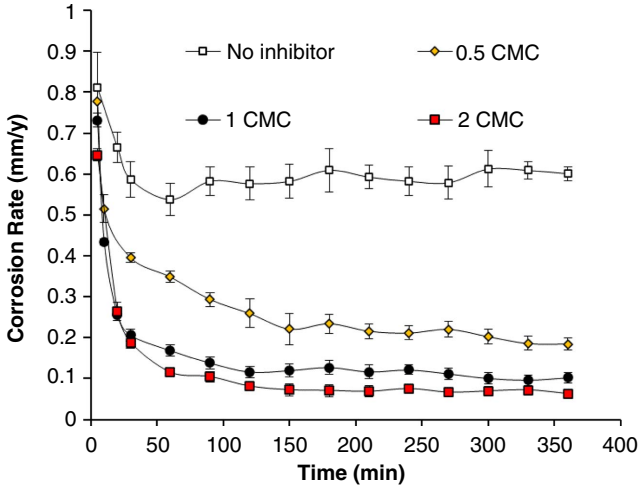

FIGURE 5. *LPR corrosion rates with time at various inhibitor concentrations for a CO_2 saturated 1 wt% NaCl aqueous electrolyte. The error bar shows the minimum and maximum values from multiple tests. Experimental conditions: 25°C, initial pH 3.9.*

3.3.2 | Atomic Force Microscopy Imaging of the Corroding Steel Surface Topography in the Absence of Inhibitor

The topography change of the steel surface immersed in 1 wt% NaCl aqueous electrolyte in the absence of an inhibitor is presented in Figure 6. The immersion time described in the text is the start time of each AFM image scan. Figure 6(a) shows the image of the initial mild steel substrate before it is exposed to the solution. Only polishing lines can be observed on the surface when the steel sample was imaged in air. Figure 6(b) shows the topography of the steel surface after 10 min of exposure in the 1 wt% NaCl aqueous electrolyte in the absence of inhibitor. It can be seen that the steel surface immediately displayed some new features, specifically, domains that are relatively higher than the surrounding surface.

These newly formed features are related to cementite (Fe_3C), which is an inherent part of the steel and is laid bare by corrosion leading to a rapid dissolution of the surrounding ferritic matrix. The UNS G10180 has a bi-phase ferrite-pearlite microstructure,[44] wherein pearlite itself is a two-phase structure with lamellar cementite situated in a ferrite matrix,[45-46] forming a well-distributed network on the steel. From the corrosion point of view, the Fe_3C present in pearlite phase is nobler than the ferrite phase (α-Fe) and remains inert, and acts as a cathodic site for the hydrogen evolution process.[47] As a consequence, iron dissolved preferentially from the ferrite phase (from matrix and pearlite), leaving the cathodic region (lamellar Fe_3C) intact,[48–49] which is shown on AFM images as elevated areas (Figure 6[b]).

With prolonged exposure (images provided in Figures 6[c] and [d] for 1 h and 4 h, respectively) polishing lines originally seen on the fresh steel surface gradually disappeared. The average height difference between inert cementite and the corroded surrounding ferrite phases increased with exposure time as ferrite dissolved continuously. According to the surface profiles shown in Figures 6(b) through (d), the height difference between the pearlite structure and surrounding ferrite is about 20±10 nm after exposure to the corrosive solution for 10 min, after a 1 h exposure this height difference becomes about 90±30 nm. About 3 h later, the height difference is ca. 260±30 nm.

Assuming that the height difference between inert cementite regions and corroded ferrite can be taken as a measure of the time-averaged local corrosion rate, it is estimated from surfaces topography profiles shown in Figures 6(b) and (c) and Equation (1) that the average corrosion rate between 10 min and 1 h is 0.7±0.2 mm/y. Similarly, from Figures 6(c) and (d), the time-averaged local corrosion rate from 1 h to 4 h exposure is estimated as 0.5±0.2 mm/y, which is in the range of the surface averaged corrosion rate as measured by LPR of 0.6± 0.1 mm/y. Reproducibility of this method for corrosion rate estimation from AFM images has been ascertained by repeating measurements with different steel specimens, and error bars of estimated corrosion rates for the first hour and 1 h to 4 h have been provided in Figure S6 (Supplemental Material).

$$\text{Corrosion rate} = \frac{90\ \text{nm} \pm 30 - 20\ \text{nm} \pm 10}{50}\text{min} \times 60\left(\frac{\text{min}}{\text{h}}\right) \times 24\left(\frac{\text{h}}{\text{d}}\right) \times \frac{365\left(\frac{\text{d}}{\text{y}}\right)}{10^{6\left(\frac{\text{nm}}{\text{mm}}\right)}} = 0.74 \pm 0.2\ \text{mm/y} \quad (1)$$

3.3.3 | Atomic Force Microscopy Imaging of the Corroding Steel Surface Topography in the Presence of BDA-C14 Inhibitor at a 0.5 CMC Bulk Concentration

A sequence of EC-AFM topography images was also collected on the same steel surface at various exposure times in 1 wt% NaCl aqueous electrolyte in the presence of inhibitor at various concentrations. At the 0.5 CMC bulk concentration, there were regions of the surface that were protected and others that were not. Figure 7 displays the topography images of a typical unprotected region on the steel surface and reveals a corrosion behavior similar to the one observed in an aqueous solution in the absence of an inhibitor (see Figure 6). As presented in Figures 7(b) and (c), sustained corrosion of the ferrite phase was revealed by the continuous decrease of surface height in the ferrite region with time, while at the same time the cementite structures were conserved as in the original steel surface. Based on the surface topography profiles in Figures 7(a) through (c), the height differences between the pearlite structure and surrounding ferrite are about 16±8 nm, 90±30 nm, and 300±60 nm, respectively, after exposure to the 0.5 CMC inhibitor solution for 10 min, 1 h, and 4 h, respectively. It is estimated from these height difference values and Equation (1) that the corrosion rate between 10 min and 1 h is 0.8±0.2 mm/y and the time-averaged local corrosion rate from 1 h to 4 h exposure is estimated as 0.6±0.3 mm/y, which are of the same magnitude as those estimated for an inhibitor-free solution as reported above. It could be therefore inferred that this region was not protected at all, as it was either bare or was covered by a disordered and loose inhibitor layer that offered little or no protection.

Figure 8 shows an example of the surface topography of an inhibited, well-protected, region of the steel surface in the presence of inhibitor BDA-C14 at a 0.5 CMC bulk concentration. Figure 8(a) shows the mild steel surface before exposure to the aqueous solution. After 10 min in this solution, slight corrosion of α-Fe has occurred, as revealed by the appearance of cementite lamellae. Nevertheless, there was no further obvious change in surface topography with an increased exposure time of 4 h, as can be observed in Figure 8(c).

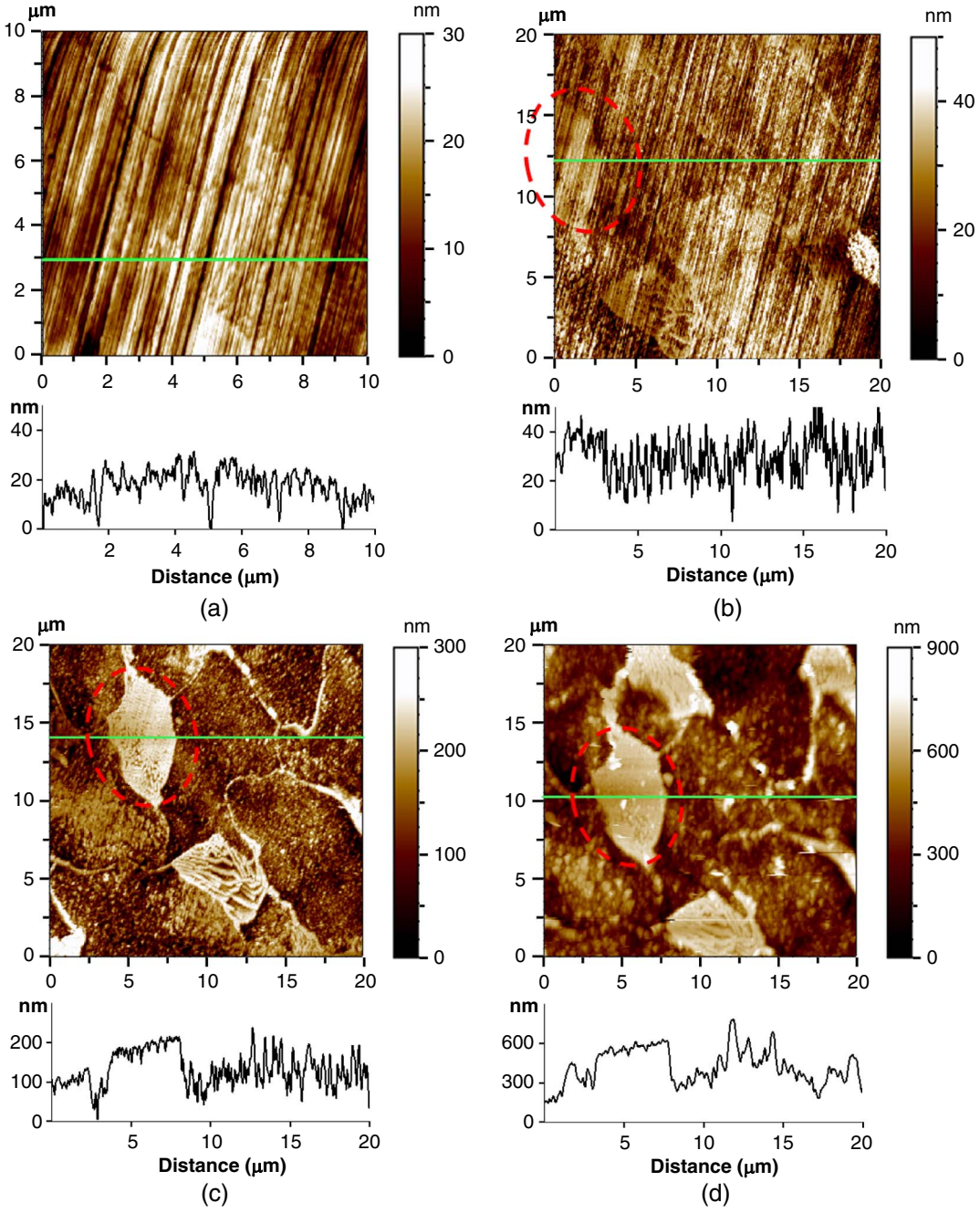

FIGURE 6. *EC-AFM monitoring of carbon steel topography: (a) in air; (b) through (d) in a CO_2 saturated 1 wt% NaCl aqueous electrolyte after (b) 10 min, (c) 1 h, and (d) 4 h exposure times. Height profiles were plotted along the green line appearing at the corresponding topography image. Experimental conditions: 25°C, initial pH 3.9. The scan rate here is set to be twice the general scan rate in In Situ Contact Mode Atomic Force Microscopy Measurements section in order to capture the fast-changed surface.*

The slight corrosion seen in Figure 8(b) after 10 min can be attributed to the inhibitor adsorption kinetics. Within the first few minutes of exposing the steel surface to an inhibited solution, the inhibitor kept on adsorbing and it took some time before it was able to form a SAM, so that in this period the ferrite corroded somewhat, leaving the striped cementite lamellae behind (Figure 8[b]). Between 10 min and 4 h, no further changes in the steel surface were observed, and it can be safely assumed that in this period the inhibitor adsorbed on this part of the steel surface and formed a SAM, which prevented the further dissolution of the ferrite phase. This is consistent with the corrosion inhibition kinetics detected by LPR (shown in Figure 5 above), where the most rapid decrease in the corrosion rate was seen in the first 10 min to 20 min.

Based on these AFM images obtained at 0.5 CMC bulk concentration, nonuniform coverage by the inhibitor was indicated, through evidence of nonuniform corrosion on the mild steel surface, which is qualitatively similar to what was seen on mica under comparable conditions. Multiple experiments have been conducted in order to establish repeatability, with the same results. An AFM image taken at the

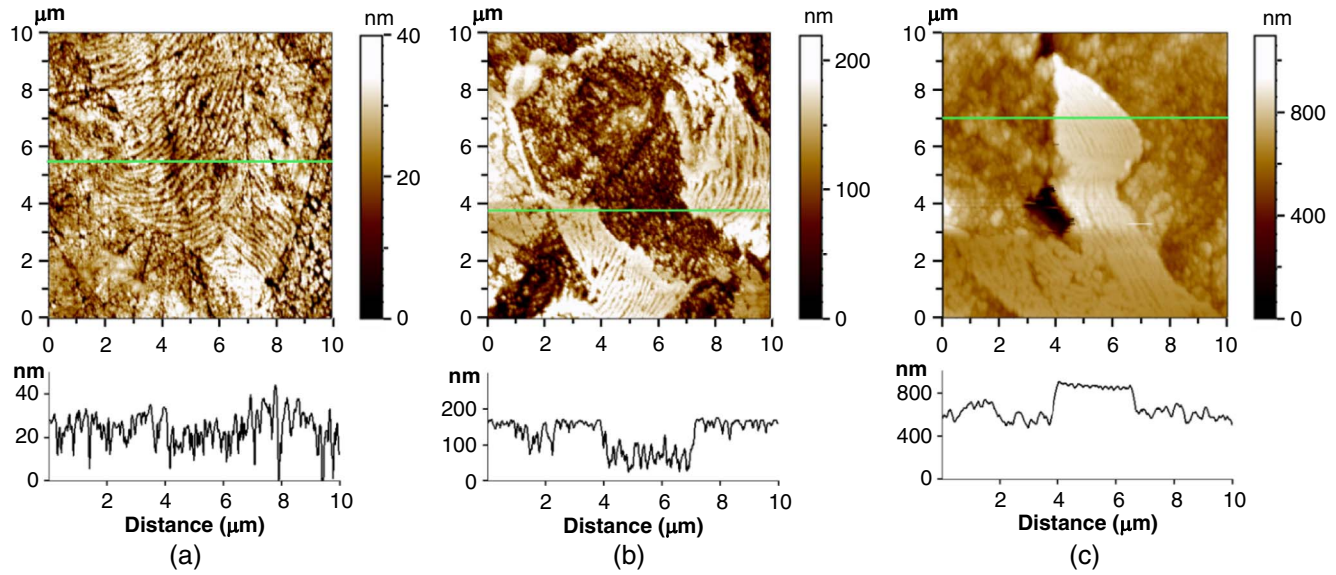

FIGURE 7. *EC-AFM monitoring of carbon steel surface topography (example of a weakly protected region) in a CO_2 saturated 1 wt% NaCl aqueous electrolyte in the presence of inhibitor at 0.5 CMC after: (a) 10 min, (b) 1 h, and (c) 4 h exposure times. Height profiles were plotted along the green line appearing at the corresponding topography image. Experimental conditions: 25°C, initial pH 3.9.*

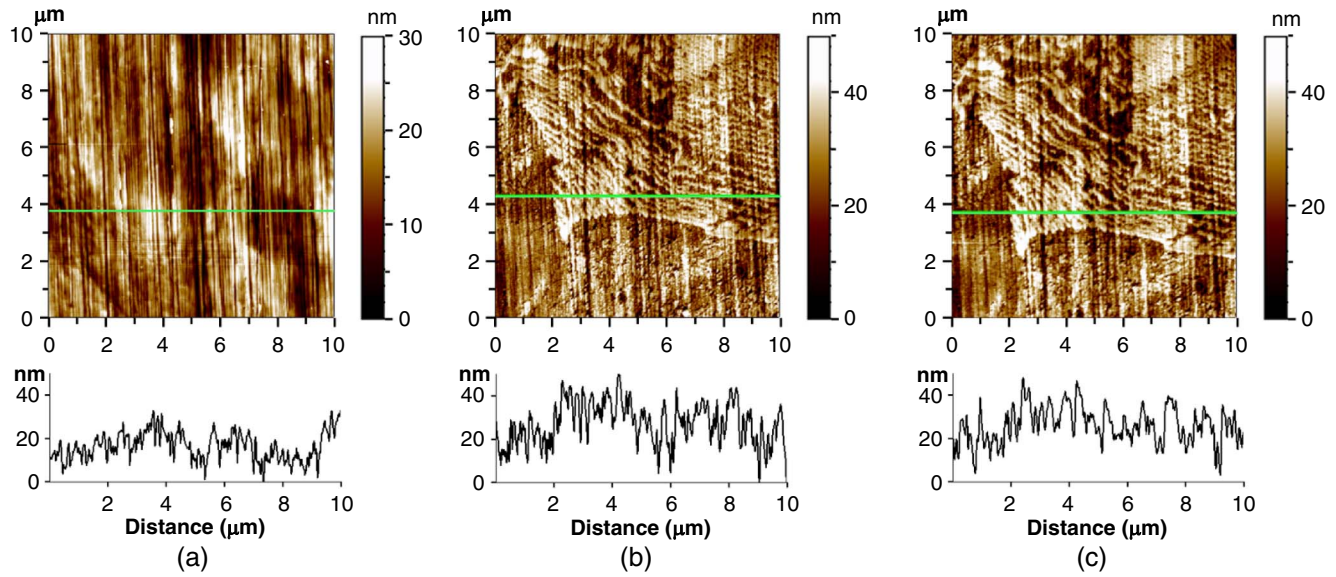

FIGURE 8. *EC-AFM monitoring for carbon steel surface topography (example of a well-protected region): (a) in air; (b,c) in a CO_2 saturated 1 wt% NaCl aqueous electrolyte in the presence of inhibitor at 0.5 CMC after (b) 10 min and (c) 4 h exposure times. Height profiles were plotted along the green line appearing at the corresponding topography image. Experimental conditions: 25°C, initial pH 3.9*

boundary region is provided in the Supplemental Material as Figure S7 which clearly shows the nonuniform coverage features with half surface protected and half surface corroded. Due to the high magnification and small field of view of the AFM, it was difficult to estimate the size of these well-protected and poorly protected regions on the steel surface with this technique. Therefore, after the AFM experiments, the steel samples immersed for 4 h in the 0.5 CMC aqueous solution were transferred to an SEM chamber for surface characterization. Figure 9(b) shows an example of the topography of an unprotected region at approximately the same magnification as the one used in the AFM images shown in Figures 7 and 8. Similar topography is observed with significant corrosion of the ferrite phase and the cementite structures remaining unchanged. The SEM image of a protected region (Figure 9[c]) indicates some slight corrosion by the appearance of cementite morphologies. However, polishing lines can still be seen clearly on the steel surface, revealing that further dissolution of ferrite was prevented with a longer exposure (4 h). The SEM image obtained at a lower magnification (Figure 9[a]) indicates a boundary between a weakly protected (highly corroded) region and a well-protected (barely corroded) region, confirming the partial protection behavior of the BDA-C14 inhibitor at 0.5 CMC concentration and nonuniform corrosion of the steel surface. The diameter of these patches was of the order of a few hundred microns.

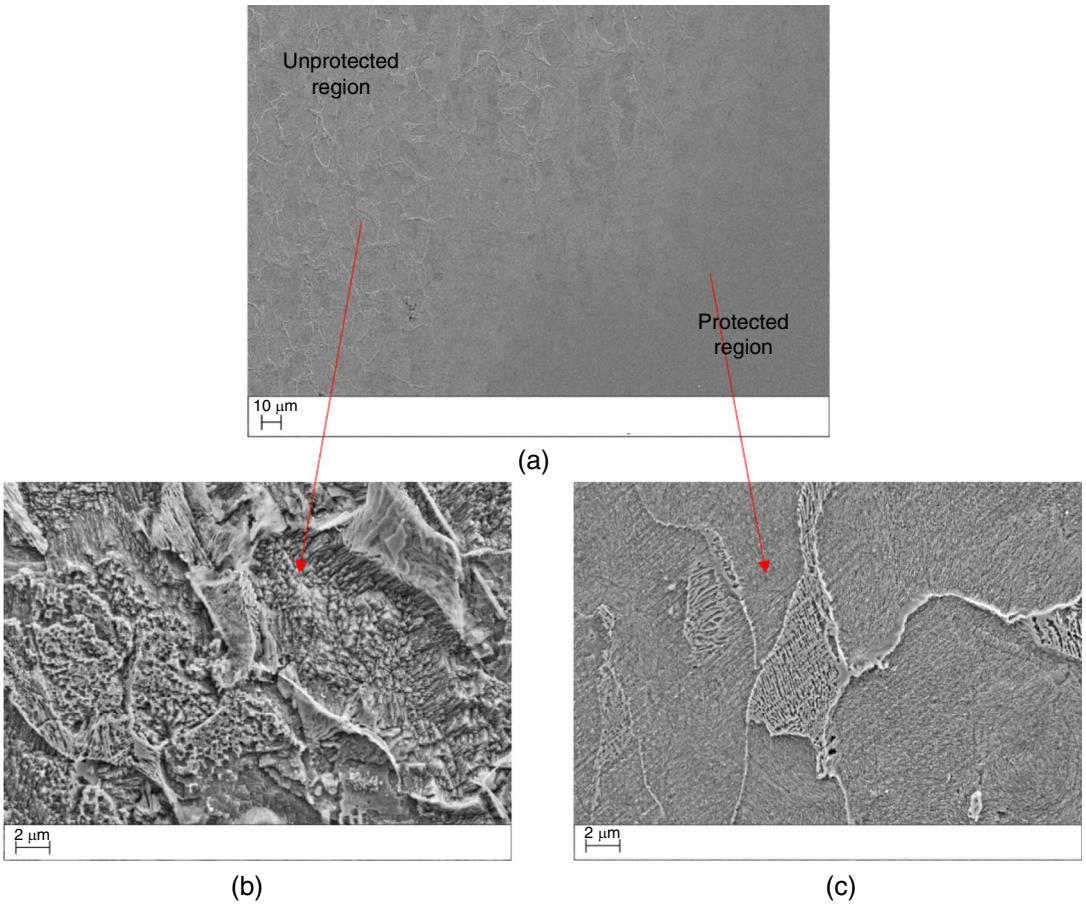

FIGURE 9. *Ex situ SEM images of the steel specimen used for EC-AFM imaging (see Figures 7 and 8) after a 4 h exposure in a CO_2 saturated 1 wt % NaCl aqueous elecrolyte containing 0.5 CMC BDA-C14 inhibitor: (a) lower magnification of a boundary between weakly protected and well-protected regions, (b) higher magnification, weakly protected region, and (c) higher magnification, well-protected region. Experimental conditions 25°C, initial pH 3.9.*

3.3.4 | Atomic Force Microscopy Imaging of the Corroding Steel Surface Topography in the Presence of BDA-C14 Inhibitor at a 1 CMC Bulk Concentration

Figure 10 shows results for the intermediate condition of 1 CMC bulk concentration. Multiple images on different locations of the same steel surface did not show any significant or sustained corrosion. The steel surface topography at the end of the experiment either showed slight corrosion (Figure S5[c]) or no corrosion, i.e., the surface preserved essentially the same topography as that observed before the exposure. This implies that at a 1 CMC concentration, the inhibitor achieved a saturation coverage for the steel surface by forming a protective self-assembled layer, similar to what was seen at 2 CMC, described below. The slight discrepancies seen in topography on different parts of the surface (slight corrosion vs. no corrosion at all) may depend on the nucleation and kinetics of self-assembled layer formation at different locations on the surface. Considering this initial stage of adsorption was short (of the order of 10 min), after which saturation inhibitor coverage reduced the corrosion rate to an extremely low value over the entire surface of the sample, only a small variation in the surface topography was seen. However, as shown by LPR corrosion rate results (Figure 5), corrosion did not stop, it continued at a low rate (of the order of 0.1 mm/y). This translates into a total of approximately 1 µm corrosion depth over the 4 d, something that could not be clearly identified in the AFM images due to short exposure durations.

3.3.5 | Atomic Force Microscopy Imaging of the Corroding Steel Surface Topography in the Presence of BDA-C14 Inhibitor at a 2 CMC Bulk Concentration

Figure 11 displays the surface topography of mild steel images using EC-AFM in the presence of an inhibitor at a 2 CMC bulk concentration. The topography is similar to that observed at 1 CMC. If it is assumed that the adsorption of the inhibitor reached a saturation coverage with a protective self-assembled layer at 1 CMC, then it is logical that the same behavior was also obtained at 2 CMC. This is consistent with the LPR measurements shown in Figure 5, where similar final corrosion rates are measured for both 1 CMC and 2 CMC bulk concentrations.

Interestingly, the corrosion kinetics of UNS G10180 steel, and its variation as a function of the bulk concentration of inhibitor, can reasonably be related to the adsorption mechanism of the inhibitor as revealed by molecular simulations applied to polar surfaces. Whatever the bulk concentration of the inhibitor, LPR measurements reveal in a first step a fast decrease of the corrosion rate that could result from the nucleation and ongoing growth of patches (islands) formed by the adsorption of an inhibitor, according to molecular

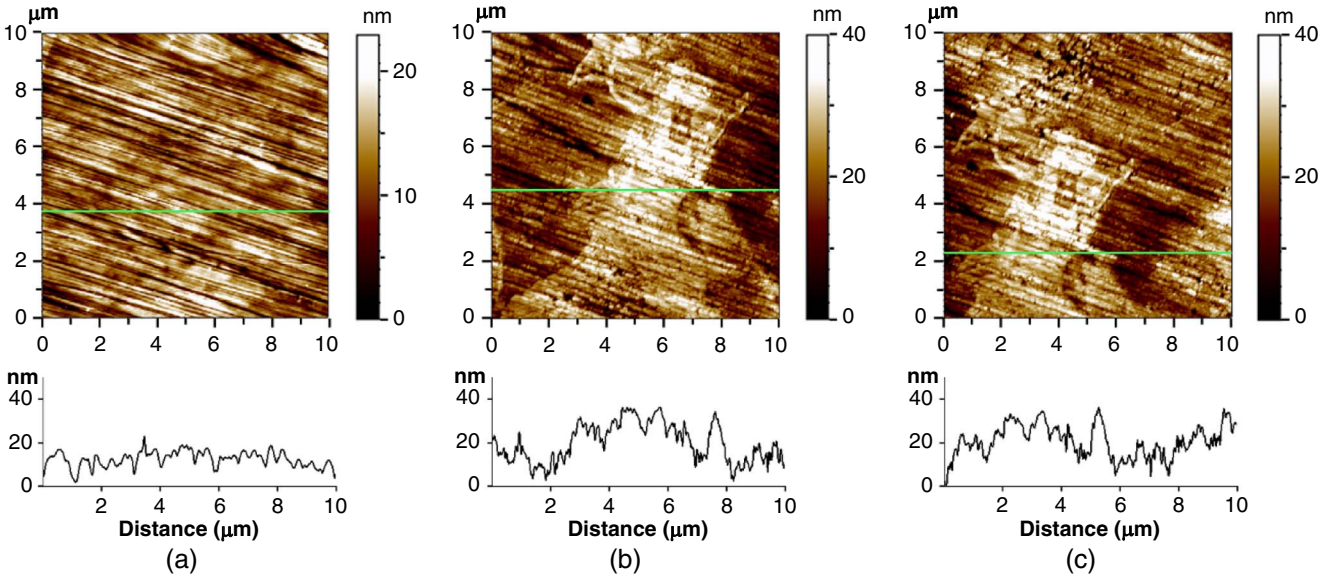

FIGURE 10. *In situ monitoring of steel morphology (case of a protected region) by AFM (a) in air, (b, c) in a 1 wt% NaCl aqueous solution in the presence of inhibitor at 1 CMC after (b) 10 min, (c) 4 h exposure time. In the profiles, the y axis shows the heights in nm as a function of distance in µm measured along the green line shown in the corresponding AFM topography image.*

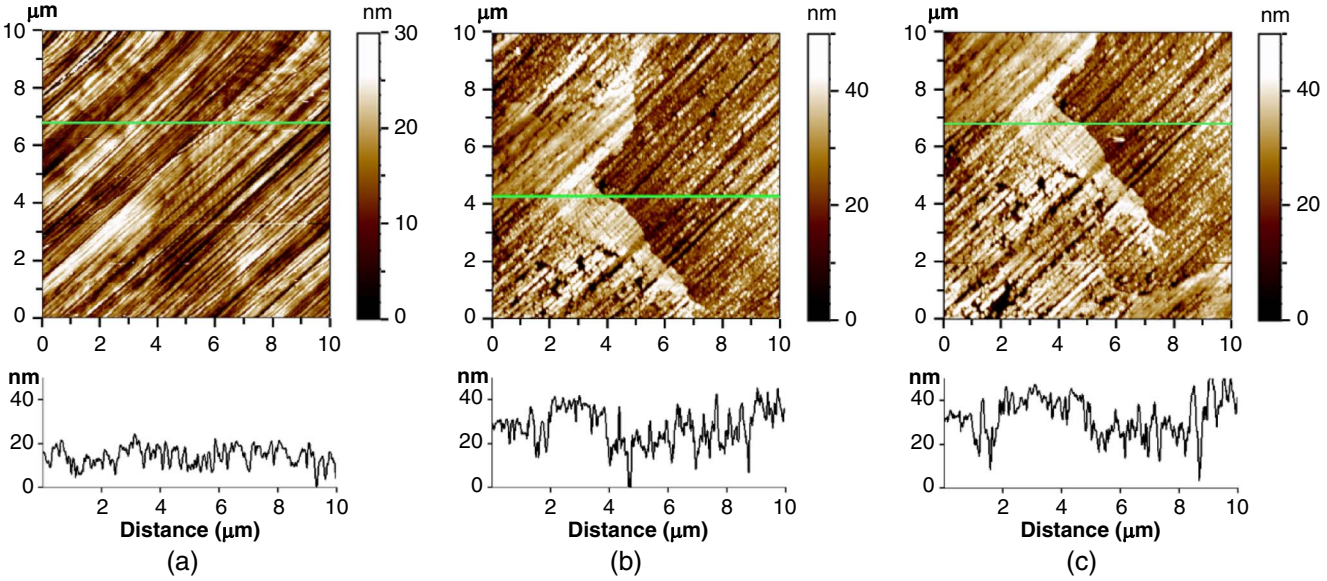

FIGURE 11. *In situ monitoring of steel topography (case of a protected region) by AFM (a) in air, (b, c) in a 1 wt% NaCl aqueous solution in the presence of inhibitor at 2 CMC after (b) 10 min, and (c) 4 h exposure time. In the profiles, the y axis shows the heights in nm as a function of distance in µm measured along the green line shown in the corresponding AFM topography image.*

simulations. LPR measurements also allowed identification, in a second step, of a steady-state corrosion rate that is lower when the bulk inhibitor concentration is higher. This second step could correspond to a stage where initially formed adsorbed inhibitor patches have coalesced together to form a single and uniform inhibitor adsorbed layer, as revealed again by molecular simulations. EC-AFM experiments have revealed that such situations can be reached at a bulk inhibitor concentration of 1 CMC and higher. At 0.5 CMC, inhibitor islands formed and resulted in nonuniform coverage, i.e., a patchwork of well-covered regions and weakly covered regions, resulting in a high corrosion rate (space-averaged) as evidenced by LPR measurements.

CONCLUSIONS

➢ In this research, in situ AFM and EC-AFM experiments were performed on mica and UNS G10180 steel, respectively, in order to develop a better understanding of the adsorption mechanism of a model inhibitor compound: tetradecyldimethylbenzylammonium (BDA-C14) at different bulk concentrations. On the basis of these experimental results and corresponding molecular simulations reported in this work, several conclusions can be drawn.

➢ The BDA-C14 corrosion inhibitor shows concentration-dependent surface coverages and adsorption behavior on both mica and carbon steel substrates, which can be correlated. At a 0.5 CMC bulk concentration, in situ AFM studies performed on mica indicate that the BDA-C14 forms a nonuniform tilted

monolayer. This observation can be correlated with what has been found on UNS G10180 steel, a partial protection phenomenon involving a patchwork of weakly protected and well-protected regions observed at the same bulk inhibitor concentration by EC-AFM. The simultaneous LPR corrosion rate measurements also reveal the steady-state corrosion rate at 0.5 CMC is greater than those obtained at higher inhibitor concentrations. The molecular simulation results are helpful to explain this phenomenon as they demonstrate that the adsorption of inhibitor molecules goes through two phases: nucleation and island growth, leading eventually to larger inhibitor islands whose size and population could be limited by bulk inhibitor concentration.

➢ Furthermore, in situ AFM studies were performed to show that, for a 2 CMC inhibitor concentration, a uniform BDA-C14 tilted bilayer or perpendicular monolayer forms on the mica surface. Parallel EC-AFM studies prove that UNS G10180 steel undergoes a uniform and slow corrosion phenomenon across its entire surface, indicating a uniformly efficient protection performance of the BDA-C14 inhibitor (similar to that obtained at 1 CMC). This is related to the saturation coverage of the UNS G10180 steel by the inhibitor layer. This high protection efficiency was confirmed by LPR measurements. Molecular simulations also confirmed that BDA-C14 islands could coalesce together to form a uniform adsorbed layer when the inhibitor bulk concentration is high.

➢ Further experiments are currently underway to strengthen and deepen the understanding of the inhibition mechanism of UNS G10180 steel corrosion by BDA-C14 as well as the evaluation of the performance of this inhibitor by comparison with other common corrosion inhibitor molecule types.

ACKNOWLEDGMENTS

The authors would like to thank the following companies for their financial support: Anadarko, Baker Hughes, BP, Chevron, CNOOC, ConocoPhillips, DNV GL, ExxonMobil, M-I SWACO (Schlumberger), Multi-Chem (Halliburton), Occidental Oil Company, Saudi Aramco, Shell Global Solutions, SINOPEC (China Petroleum), and TotalEnergies. This work is partially supported by National Science Foundation CBET Grant 1705817. The computational resources for this work were provided by the Ohio Supercomputer Center and National Science Foundation XSEDE Grant No. DMR190005. The authors also would like to thank Dr. David Young for synthesizing the corrosion inhibitor model compound used in this work and also for help with manuscript reviewing, Dr. Xueying Ko for help analyzing the simulation results, Dr. Zineb Belarbi for helping find references to interpret AFM data and also providing AFM operation training, and Dr. Juan Dominguez Olivo for helping in interpreting the electrochemical data.

References

1. S. Papavinasam, "Corrosion Inhibitors," *Uhlig's Corrosion Handbook* (Hoboken, NJ: Wiley, 2011), p. 1021-1032.
2. J. Carrasco, A. Hodgson, A. Michaelides, *Nat. Mater.* 11 (2012): p. 667-674.
3. A. Edwards, C. Osborne, S. Webster, D. Klenerman, M. Joseph, P. Ostovar, M. Doyle, *Corros. Sci.* 36, (1994), p. 315-325.
4. C. Cao, *Corros. Sci.* 38 (1996): p. 2073-2082.
5. W. Lorenz, F. Mansfeld, *Electrochim. Acta* 31 (1986): p. 467-476.
6. M. Veloz, I. Martínez, *Corrosion* 62 (2006): p. 283-292.
7. X. Chen, W. Dong, X. Zhang, *Sci. China Chem.* 53 (2010): p. 1853-1861.
8. H.N. Patrick, G.G. Warr, S. Manne, I.A. Aksay, *Langmuir* 15 (1999): p. 1685-1692.
9. S. Manne, T. Schäffer, Q. Huo, P. Hansma, D. Morse, G. Stucky, I.A. Aksay, *Langmuir* 13 (1997): p. 6382-6387.
10. X. Ko, S. Sharma, *J. Phys. Chem. B* 121 (2017): p. 10364-10370.
11. S. Sharma, X. Ko, Y. Kurapati, H. Singh, S. Nešić, *Corrosion* 75 (2019): p. 90-105.
12. J. Woodward, I. Doudevski, H. Sikes, D. Schwartz, *J. Phys. Chem. B* 101 (1997): p. 7535-7541.
13. D.K. Schwartz, S. Steinberg, J. Israelachvili, J.A.N. Zasadzinski, *Phys. Rev. Lett.* 69 (1992): p. 3354.
14. I. Doudevski, W.A. Hayes, D.K. Schwartz, *Phys. Rev. Lett.* 81 (1998): p. 4927.
15. W.A. Hayes, D.K. Schwartz, *Langmuir* 14 (1998): p. 5913-5917.
16. M. Jaschke, H.-J. Butt, H. Gaub, S. Manne, *Langmuir* 13 (1997): p. 1381-1384.
17. G. Poirier, E. Pylant, *Science* 272 (1996): p. 1145-1148.
18. I. Jevremović, M. Singer, S. Nešić, V. Mišković-Stanković, *Corros. Sci.* 77, (2013), p. 265-272.
19. B. Wang, M. Du, J. Zhang, C.J. Gao, *Corros. Sci.* 53, 1 (2011): p. 353-361.
20. J.D. Olivo, B. Brown, S. Nešić, "Modeling of Corrosion Mehcanisms in the Presence of Quaternary Ammonium Chloride and Imidazoline Corrosion Inhibitors," CORROSION 2016, paper no. 7406 (Houston, TX: NACE, 2016), p. 1.
21. N. Moradighadi, S. Lewis, J.D. Olivo, D. Young, B. Brown, S. Nešić, *Corrosion* 77 (2021): p. 266-275.
22. J.D. Olivo, B. Brown, D. Young, S. Nešić, *Corrosion* 75 (2019): p. 137-139.
23. F. Ostendorf, C. Schmitz, S. Hirth, A. Kühnle, J.J. Kolodziej, M. Reichling, *Nat. Nanotechnol.* 19 (2008): p. 305705.
24. T. Balmer, H. Christenson, N. Spencer, M. Heuberger, *Langmuir* 24 (2008): p. 1566-1569.
25. B.-B. Lee, P. Ravindra, E.-S. Chan, *Colloids Surf. A* 332 (2009): p. 112-120.
26. F.E. Ala'a, M.F. Paige, *J. Colloid Interface Sci.* 353 (2011): p. 210-219.
27. Y. Xiong, B. Brown, B. Kinsella, S. Nešić, A. Pailleret, *Corrosion* 70 (2014): p. 247-260.
28. Z. Belarbi, B. Brown, M. Singer, S. Nešić, "Study of Adsorption of Corrosion Inhibitor 1-(2-Aminoethyl)-2-Oleyl-2-Imidazolinium Chloride on Carbon Steel Under CO_2 Environment by Using in situ AFM Measurements," CORROSION 2017, paper no. 9290 (Houston, TX: NACE, 2017), p. 1.
29. W. Li, B. Pots, X. Zhong, S. Nešić, *Corros. Sci.* 126 (2017): p. 208-226.
30. M.G. Allen, S.D. Senturia, *J. Adhes.* 29 (1989), p. 219-231.
31. J. Wang, R.M. Wolf, J.W. Caldwell, P.A. Kollman, D.A. Case, *J. Comput. Chem.* 25 (2004): p. 1157-1174.
32. L. Wang, J. Jiang, Y. Song, B. Zhang, E. Wang, *Langmuir* 19 (2003): p. 4953-4957.
33. N. Kovačević, I. Milošev, A. Kokalj, *Corros. Sci.* 124 (2017): p. 25-34.
34. M.R. Khan, H. Singh, S. Sharma, *J. Phys. Chem. Lett.* 11, 22 (2020): p. 9901-9906.
35. Y. Yao, L. Qiao, A.A. Volinsky, *Corros. Sci.* 53 (2011): p. 2679-2683.
36. A.M. Siitonen, K. Sumitomo, C.S. Ramanujan, Y. Shinozaki, N. Kasai, K. Furukawa, J.F. Ryan, K. Torimitsu, *Appl. Surf. Sci.* 254 (2008): p. 7877-7880.
37. X. Liang, G. Mao, K.S. Ng, *J. Colloid Interface Sci.* 278 (2004): p. 53-62.
38. J. Zhang, J. Liu, W. Yu, Y. Yan, L. You, L. Liu, *Corros. Sci.* 52 (2010): p. 2059-2065.
39. S. Sharma, H. Singh, X. Ko, *J. Phys. Chem. B* 123 (2019): p. 7464-7470.
40. R. Xu, B. Liu, *J. Appl. Mech.* 81 (2014).
41. M. Ester, H. P. Kriegel, J. Sander, X. Xu, Knowledge Discovery and Data Mining 1996: p. 226-231.
42. T. Murakawa, S. Nagaura, N. Hackerman, *Corros. Sci.* 7 (1967): p. 79-89.
43. N. Pebere, M. Duprat, F. Dabosi, A. Lattes, A. De Savignac, *J. Appl. Electrochem.* 18 (1988): p. 225-231.
44. J. Bulger, B. Lu, J. Luo, *J. Mater. Sci.* 41 (2006): p. 5001-5005.
45. Y. Ivanisenko, W. Lojkowski, R. Valiev, H. J. Fecht, *Acta Mater.* 51 (2003): p. 5555-5570.
46. L.D. Paolinelli, T. Pérez, S.N. Simison, *Corros. Sci.* 50 (2008): p. 2456-2464.
47. B. Mishra, S. Al-Hassan, D. Olson, M. Salama, *Corrosion* 53 (1997): p. 852-859.
48. F. Farelas, M. Galicia, B. Brown, S. Nešić, H. Castaneda, *Corros. Sci.* 52 (2010): p. 509-517.
49. Z. Zhang, G. Chen, G. Chen, Mater. Eng. Sci. A 422 (2006): p. 241-251.

Investigation of corrosion inhibitor adsorption on mica and mild steel using electrochemical atomic force microscopy and molecular simulations

Huiru Wang, Sumit Sharma, Alain Pailleret, Bruce Brown, and Srdjan Nešić

https://doi.org/10.5006/4136

SUPPLEMENTAL MATERIAL

Here is the procedure of EC-AFM experiments in a CO_2 atmosphere. Firstly, the solution is deoxygenated by sparging CO_2 for at least 2 hours outside the AFM set up before experiments begin. Secondly the sample and electrochemical cell shown in Figure SM-1 were installed on the AFM equipment with a sealed homemade environmental chamber. CO_2 gas was continuously sparged in to the environmental chamber during the whole experiments to create a CO_2 atmosphere around the EC-AFM cell. The deoxygenized solution was transferred to the EC-AFM cell through a syringe to guarantee CO_2 saturated solution would not be exposed to air.

The pH was measured in a flask where the solution was saturated with CO_2 before experiments begun at 25°C, and then the solution was transferred to the EC-AFM cell inside the AFM environmental chamber and was in contact with CO_2 atomosphere immediately. During this process the pH of solution would not change because it was always CO_2 saturated at the same temperature.

Figure SM-3 shows the results of the scratching tests, where removal of the inhibitor molecules in the scratched area was achieved by gradually increasing the normal force applied by the cantilever. This procedure has been described in more details in a previous publication [1]. In particular, it has been shown that the normal force used during these scratching tests is not sufficiently high to scratch away bare mica and therefore only the adsorbed BDA-C14 molecules were removed.

When the normal force was too small to penetrate the inhibitor layer, the AFM image obtained after scratching shows the unaltered morphology of an adsorbed layer (Figure SM-3a1). When the applied force was high enough to penetrate the layer but was not large enough to remove the inhibitor molecules, some disturbance in the topography of the layer was observed (Figure SM-3b1), however the surface profile revealed that the inhibitor molecules were not removed from the scratching prints. When the force was large enough to remove the inhibitor molecules, a scratching print (hole) could be clearly observed in the topography image and in the surface profile (Figure 3a in manuscript). When the force was increased further, the depth of the scratched feature did not increase. In our experimental conditions, the layer was completely removed with a 24±1 nN operating normal force (shown in Figure 3a). Considering that mica is a hard surface, and that previous studies [1] showed that even a normal force of 60 nN did not result in any damage to the mica, we can conclude that the scratching feature (hole) seen in Figure 3a is a removed patch of inhibitor layer rather than a damaged mica surface. So, the surface profile reveals the inhibitor layer thickness.

As mentioned in the manuscript section 3.1, in some locations of the mica surface at 0.5 CMC, a positive height contrast instead of a hole (with a negative height contrast) was detected in the AFM images obtained after a nano-scratching step (see Figure SM-4). These AFM nano-scratching tests (Figure 3a and

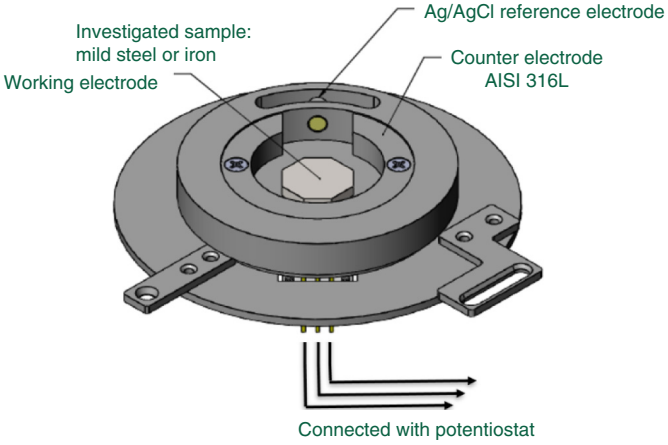

Figure SM-1: *Custom-made sample holder for EC-AFM experiments*

Table SM-1. *Elemental composition of UNS G1018 steel (Fe balance)*

Element	Al	As	C	Co	Cr	Cu	Mn	Mo
Amount (wt%)	0.008	0.006	0.18	0.003	0.12	0.18	0.75	0.02
Element	Ni	P	S	Sb	Si	Sn	Ta	W
Amount (wt%)	0.065	0.011	0.021	0.009	0.16	0.009	0.028	0.014

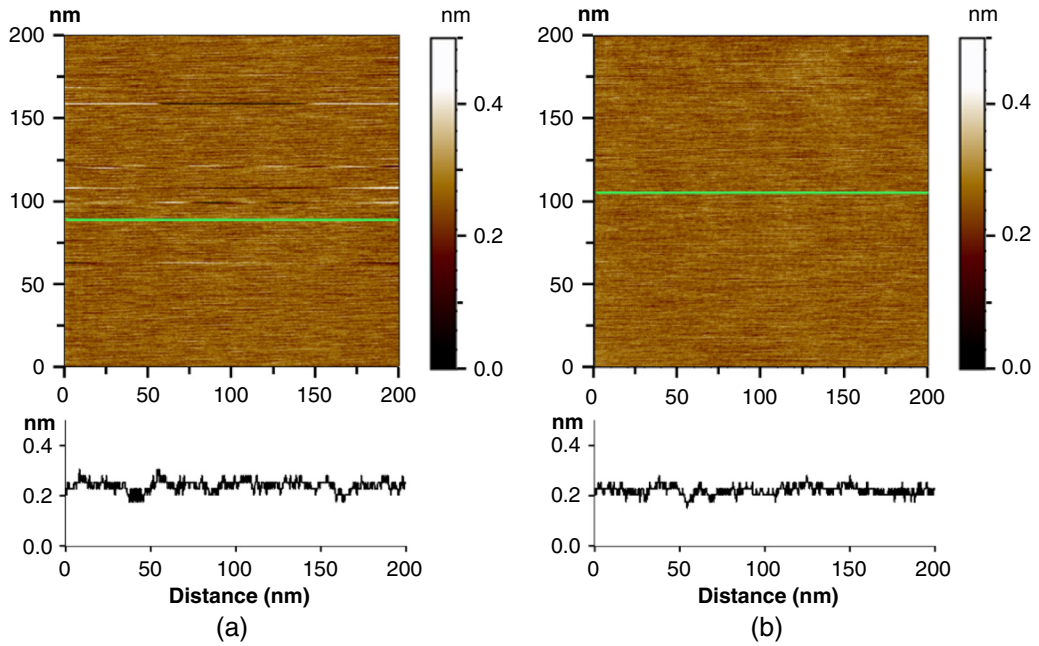

Figure SM-2: *AFM topography images and surface profiles obtained on mica in 1 wt% NaCl aqueous solutions (a) in the absence of inhibitor (b) in the presence of BDA-C14 at a 2 CMC bulk concentration. The surface roughness in both images is less than 1 Å. Height profiles were plotted along the green line appearing at the corresponding topography image.*

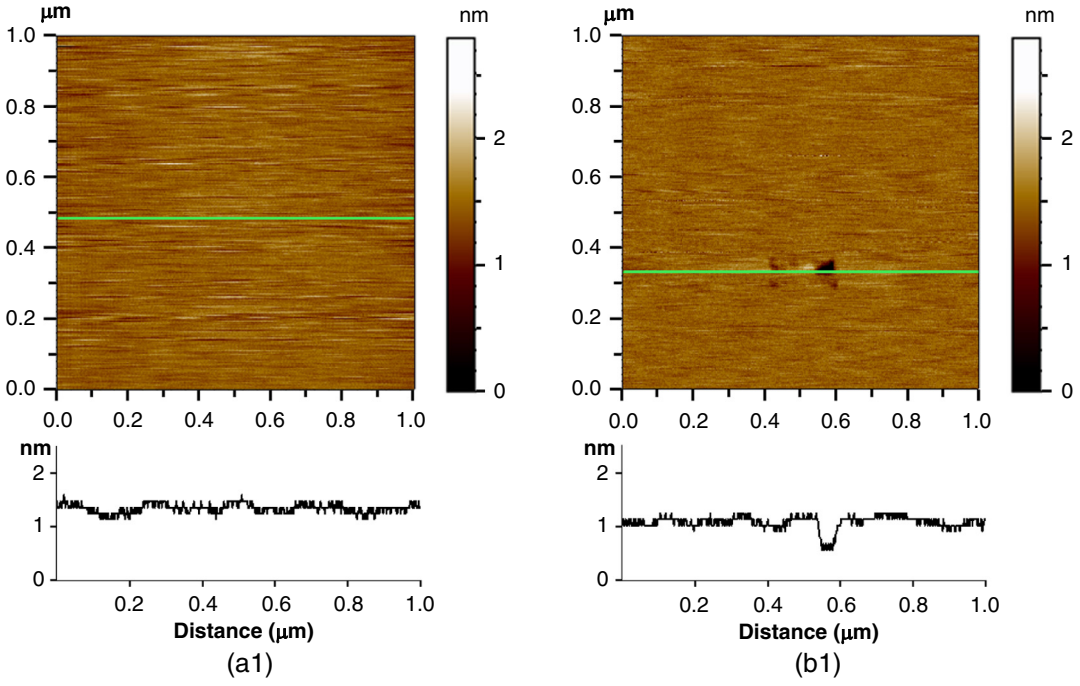

Figure SM-3: *Topography images of inhibitor layers formed on mica. At 2 CMC with various normal forces applied on cantilever: (a1) <2 nN, (b1) 21 nN. Height profiles were plotted along the green line appearing at the corresponding topography image.*

SM-4) indicate the inhibitor film formed at 0.5 CMC is non-uniform. When a AFM nanoscratching test was carried out on a portion of the surface where there was a self-assembled monolayer (SAM), the high force exerted by the AFM tip leads to layer removal and a hole was created [1,2], as shown in Figure 3a. However, when the same AFM nanoscratching test was performed on another location of the surface which was weakly covered by some adsorbed inhibitor molecules with lower density and not organized in the form of a SAM, it did not produce any hole, but rather an island [2,3], as observed in Figure SM-4. An explanation for this observation can be found in the literature related to AFM nanolithography and nano-grafting [4-7]. One can think of a scenario explaining how these islands were created during the nanoscratching test: when a high normal force is applied, the tip pushed around the inhibitor molecules that were adsorbed in a disordered way on the surface and piled them into a "heap" that

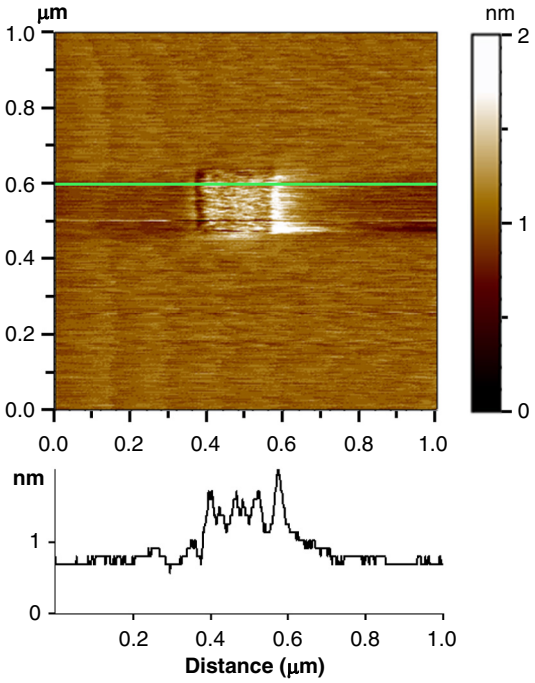

Figure SM-4: *Topography images obtained after nano-scratching steps performed on inhibitor layers formed on mica at 0.5 CMC with positive height contrast.*

was registered as an island in the AFM scan performed after the nanoscratching step. This apparently did not happen when scanning was performed with a low normal force because the force applied was not high enough for displacing the adsorbed inhibitor molecules. AFM force curves tests (discussed in the second half of section 3.1 and also in below Figure SM-5 and corresponding text) will provide further confirmation on the layer structure at different inhibitor concentrations.

The AFM force curves shown in Figure SM-5 measure the tip-sample interaction force as a function of tip-sample distance in 1 wt% NaCl solution with various BDA-C14 inhibitor concentrations. The horizontal axis represents the AFM tip/sample distance during the approach of the cantilever. The Y-axis shows the cantilever deflection which is proportional to the interaction force. For each experiment three repeating curves are displayed to address the repeatability of the observed phenomena. The Force curves were performed on bare mica in 1 wt% NaCl solution firstly as a baseline. On the bare mica surface, when the tip is far away from the sample, there is no interaction between the tip and the surface so that the force is almost zero, as shown in Figure 3 and Figure SM-5a (see the horizontal part of the curves). As the tip approaches the surface, the cantilever deflects towards the sample due to the increasing attractive van der Waals forces. Indeed, as the tip approaches the sample surface even more closely, the gradient of attractive force (will increase and finally exceeds the cantilever spring constant [8-11]. So, at a certain distance, the attractive force becomes larger than the resistive force of the cantilever [12,13], and thus the cantilever tip will "snap" into contact with the sample surface. Further approach of the AFM cantilever, pushing against a stiff mica surface, results in a rapid rise in the force curve, corresponding to a strong positive/repulsive force which increases linearly with distance, caused by the cantilever bending upwards.

The AFM force curve obtained at 2 CMC BDA-C14 solution have been analyzed in detail in manuscript (Figure 3).

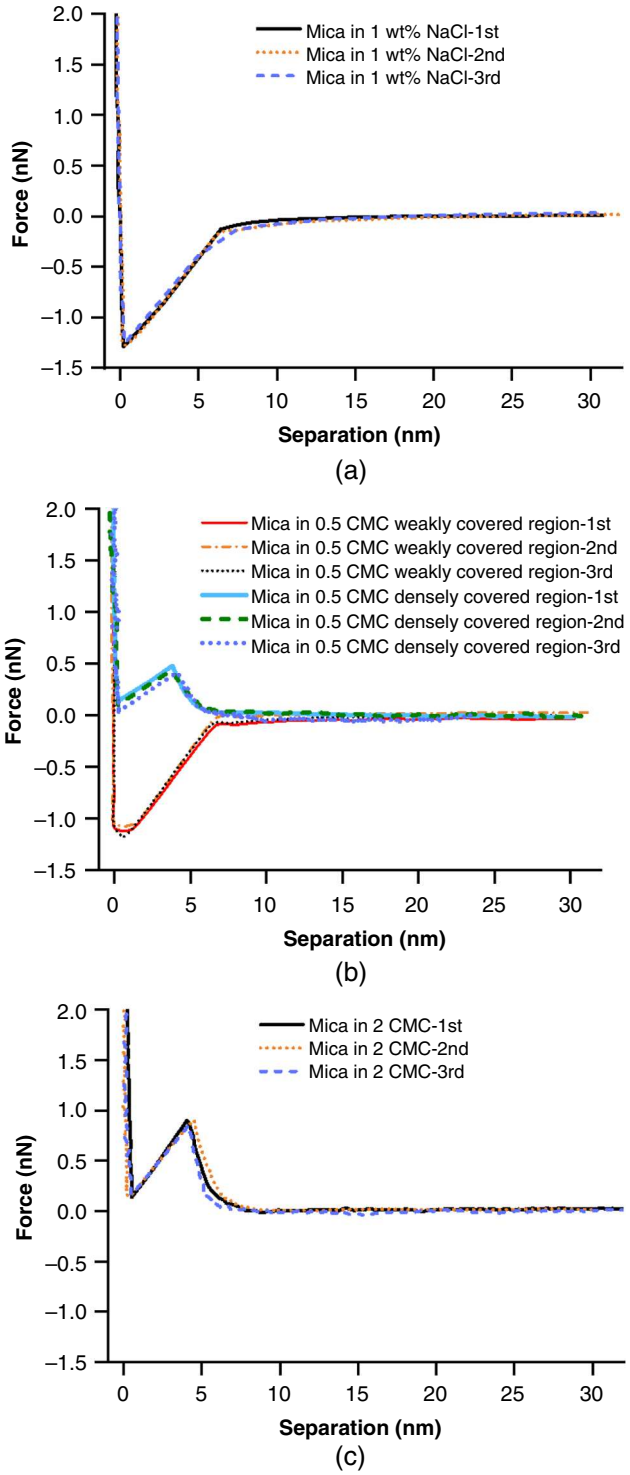

Figure SM-5: *AFM force curves obtained on mica in 1 wt% NaCl aqueous solutions (a) in the absence of inhibitor (b) in the presence of BDA-C14 at 0.5 CMC bulk concentration. Non-uniform adsorption status (covered region and non-covered region) were observed. (c) in the presence of BDA-C14 at 2 CMC bulk concentration. Reproducibility has been observed in at least three samples.*

A repulsive force feature indicating the existence of well-organized inhibitor film was observed on the force curves at 2 CMC (Figure 3 and Figure SM-5c). In the case of 0.5 CMC BDA-C14 solution (Figure SM-5b), AFM force curves corresponding to

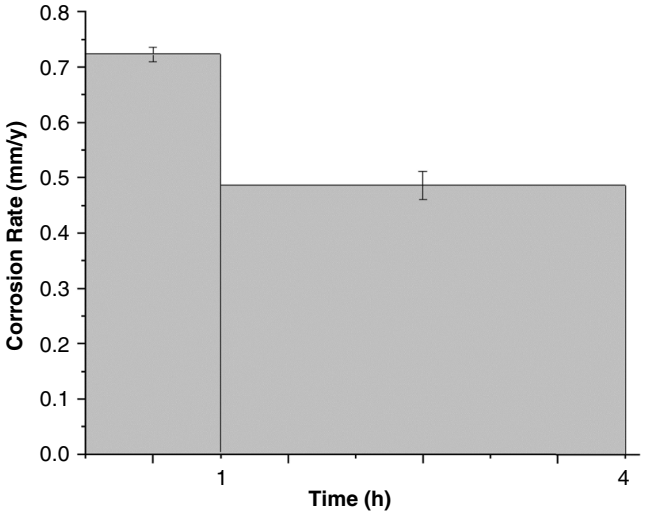

Figure SM-6: *average corrosion rate estimated from cementite-ferrite height difference in AFM surface profiles and error bar of repeating experiments for steel immersed in 1 wt% NaCl aqueous solution in the absence of inhibitor in the first hour immersion and between 1 to 4 hours immersion.*

some regions of the mica surface were qualitatively similar to those obtained in a 2 CMC solution with the curve denoted as "mica in 0.5 CMC densely covered region " (see blue solid curve). However, in other regions of the mica surface, as shown in Figure SM-5b with the curve denoted as " mica in 0.5 CMC weakly covered region" (see red solid curve), the force curve was similar to that of the bare mica surface, indicating that the adsorbed inhibitor molecules produced a weak and disordered coverage with little intermolecular interaction. These force curves results are in good agreement with the interpretation of the nano-scratching tests performed at a 0.5 CMC inhibitor concentration: a non-uniform coverage of the mica surface by the inhibitor layer is detected.

As can be seen from Figure SM-7, there exists a clear partial corrosion on UNS G10180 steel under this 0.5 CMC concentration. On the left part of the image is the protected region, which shows polishing lines still can be observed after 4 hours immersion and the surface roughness is within 20nm (similar with the polished surface before immersion). On the right part is the corroded region, the height difference between protected region and non-protected region can be up to 270±50 nm (profile a and b). Apparently the cementite structure remained noble and intact in the non-protected region, as indicated in profile b. The surface height of cementite in non-protected region is almost the same with the corroded region, while the ferrite structure in non-protected region has corroded a lot and has a much smaller height.

References

1. Y. Xiong, B. Brown, B. Kinsella, S. Nešić, A. Pailleret, Atomic force microscopy study of the adsorption of surfactant corrosion inhibitor films, *Corrosion*, 70 (2014) 247-260.
2. B. Torun, B. Ozkaya, G. Grundmeier, Atomic Force Microscopy (AFM)-based nanografting for the study of self-assembled monolayer formation of organophosphonic acids on Al2O3 single-crystal surfaces, *Langmuir*, 28 (2012) 6919-6927.
3. S. Xu, G.-y. Liu, Nanometer-scale fabrication by simultaneous nanoshaving and molecular self-assembly, *Langmuir*, 13 (1997) 127-129.
4. R.D. Piner, J. Zhu, F. Xu, S. Hong, C.A. Mirkin, "Dip-pen" nanolithography, *science*, 283 (1999) 661-663.
5. R. García, M. Calleja, H. Rohrer, Patterning of silicon surfaces with noncontact atomic force microscopy: Field-induced formation of nanometer-size water bridges, *J. Appl. Phys.* 86 (1999) 1898-1903.
6. S. Ryu, G.C. Schatz, Nanografting: Modeling and simulation, *J. Am. Chem. Soc.* 128 (2006) 11563-11573.
7. L.G. Rosa, J. Liang, Atomic force microscope nanolithography: dip-pen, nanoshaving, nanografting, tapping mode, electrochemical and thermal nanolithography, *J. Phys. Condens. Matter* 21 (2009) 483001.
8. B. Cappella, *Mechanical properties of polymers measured through AFM force-distance curves*, Springer, 2016.
9. A. Baszkin, W. Norde, *Physical chemistry of biological interfaces*, CRC Press, 1999.
10. C.L. Tinker-Mill, Nanoscale imaging and characterisation of Amyloid-β;, Springer, 2016.
11. Z. Chen, L. Huang, G. Zhang, Y. Qiu, X. Guo, Benzotriazole as a volatile corrosion inhibitor during the early stage of copper corrosion under adsorbed thin electrolyte layers, *Corros. Sci.* 65 (2012) 214-222.
12. J. Rychen, T. Ihn, P. Studerus, A. Herrmann, K. Ensslin, H. Hug, P. Van Schendel, H. Güntherodt, Force–distance studies with piezoelectric tuning forks below 4.2 K, *Appl. Surf. Sci.* 157 (2000) 290-294.
13. K. Wandelt, Surface and Interface Science, Volumes 1 and 2: Volume 1-Concepts and Methods; Volume 2-Properties of Elemental Surfaces, John Wiley & Sons, 2012.

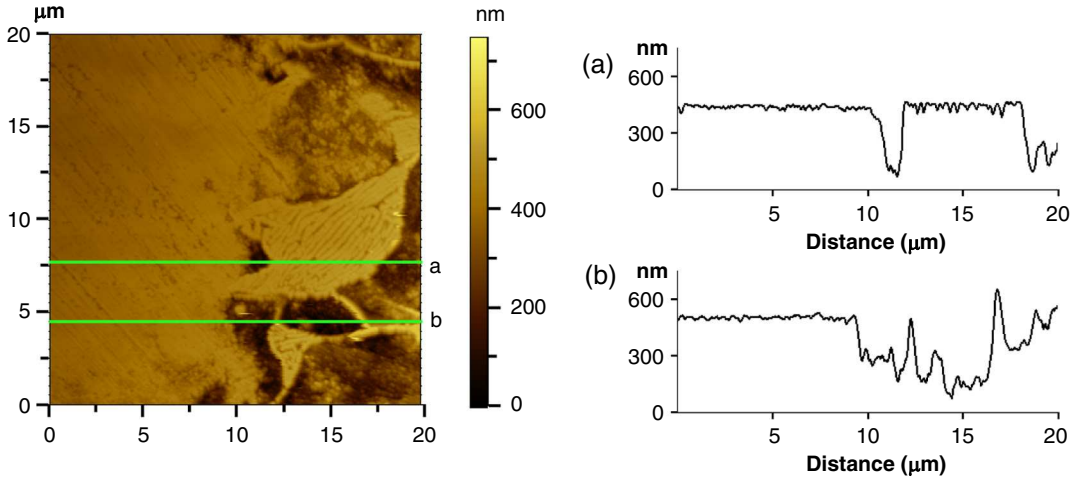

Figure SM-7: *EC-AFM topography imaging for steel in a 1 wt% NaCl aqueous solution in the presence of inhibitor at 0.5 CMC for 4 hours——the boundary region between protected area and non-protected area. Both a and b are the horizontal cross section profiles to show the surface roughness difference between protected area and non-protected area.*